J. Fluid Mech. (2009), *vol.* 629, *pp.* 109–137.
doi:10.1017/S0022112009006260 Printed in the United Kingdom

Effects of spatially varying roof cooling on thermal convection at high Rayleigh number in a fluid with a strongly temperature-dependent viscosity

A. M. JELLINEK[1]† AND A. LENARDIC[2]

[1]Department of Earth and Ocean Sciences, The University of British Columbia, Vancouver, BC V6T1Z4, Canada

[2]Department of Earth Science, Rice University, Houston, TX 77005, USA

(Received 6 April 2008 and in final form 13 January 2009)

We investigate the effects of an insulating lid of variable spatial extent on convection in the stagnant-lid regime under thermally steady-state conditions. Using a combination of laboratory experiments, numerical simulations and scaling analyses we characterize the qualitative structure and quantitative heat transfer properties of flows in terms of the fractional extent L of an insulating lid applied at the cold boundary, the thermal resistance of the lid, the magnitude of the temperature dependence of the fluid viscosity Λ and the effective Rayleigh number Ra_e for the composite system. A partial insulating lid has two main effects: (i) To increase the mean interior temperature and reduce the average viscosity of the system, which enhances fluid motions, and (ii) to impart a lateral asymmetry to the thermal structure of the cold boundary that leads, in turn, to lateral temperature gradients that drive an overturning flow. Consequently, whereas flow in the uninsulated stagnant-lid regime is in the form of 'small-scale' rising and sinking thermals, there is an additional 'large-scale' circulation in the presence of partial insulation. The structure, wavelength and heat transfer properties of this large-scale stirring depends on L, Λ and Ra_e. For given $Ra_e - \Lambda$ conditions we find optimal values of L at which there occur well-defined maxima in the rate of overturn, the local heat flux carried into the uninsulated part of the cold boundary and in the global average heat flux Nu carried across the system. Whereas both the rate of overturning and local heat flux are associated with the largest lateral temperature gradients, the optimal basal heat flux depends also on a tradeoff with the fractional surface area of the lid. Remarkably, maximal values of the global heat flux can significantly exceed that of the uninsulated stagnant-lid case. The occurrence of such maxima is insensitive to the mechanical boundary conditions applied and is not strongly influenced by lid shape. However, the magnitude and location of optimal heat fluxes depends in a complicated way on the lid surface area and shape, as well as the structure of the hot and cold boundary layers and the wavelength of the large-scale flow.

† Email address for correspondence: mjellinek@eos.ubc.ca

1. Introduction

Natural thermal convection in fluids with strongly temperature-dependent viscosities plays an important role in many problems in Earth and planetary sciences. Examples include the thermal evolution of planetary mantles, the growth and differentiation of magma chambers, the circulation of hydrothermal brines and ore genesis. In many such problems a fluid layer is heated from below and cooled from above, analogous to classical Rayleigh–Bénard convection with homogeneous isothermal (or constant heat flux) upper and lower boundaries. An additional class of problems involves spatially varying surface cooling, arising due to the presence of an insulating layer separating a convecting fluid either partially or completely from a cold reservoir to which it is cooling. Natural occurrences of this phenomena are varied and arise in a number of situations. Examples include the insulating effect of continents on mantle convection in the Earth (e.g. Gurnis 1988; Zhong & Gurnis 1993; Guillou & Jaupart 1995; King & Ritsema 2000; Grigne & Labrosse 2001; Lenardic & Moresi 2003; Korenaga & Jordan 2004; Grigne, Labrosse & Tackley 2005; Lenardic *et al.* 2005), spatially irregular porous media flow in geothermal areas such as mid-ocean ridges (e.g. Lister 1972; Elder 1981; Hartline & Lister 1981; Donaldson 1982; Norton 1984; Davis & Chapman 1989; Lister 1990*a*,*b* 1995; Lowell & Burnell 1991), porous media flow in sedimentary basins (e.g. Lister 1990; Person *et al.* 1996) and the effect of sea ice on heat transfer from the oceans to the atmosphere (Parkinson *et al.* 1987; Aargard & Carmack 1989; Hibler 1989; Gloersen *et al.* 1992), which can strongly influence the global climate system (e.g. Aargard & Camack 1994; Parkinson 1997).

Qualitatively, previous experimental studies of convection at high Rayleigh (i.e. $Ra \geqslant O(10^6)$) numbers have shown that lateral temperature variations related to a partial insulating lid can influence the structure, wavelength and thermal properties of the flow (Guillou & Jaupart 1995; Zhang & Libchaber 2000). In a recent two-dimensional numerical study of mantle convection on Earth Lenardic *et al.* (2005) find a particularly unintuitive consequence of partial insulation: Insulating continents can enhance the rate of global mantle cooling over the continent-free situation, depending on the surface area of continents and the mantle rheology. A scaling analysis shows that provided the temperature-dependence of the mantle viscosity is large the presence of continents raises the average internal mantle temperature, which, in turn, lowers the viscosity of the system and increases the rate of subduction and mantle overturning. Thus, depending on a tradeoff with the surface area of continents, which governs the area through which heat can be transferred from the mantle to the atmosphere, the presence of continents can augment the cooling of the Earth.

In their analysis, Lenardic *et al.* (2005) explore the effects of partial insulation on a basic state of 'active lid' mantle convection that is driven by the subduction and stirring of the cold boundary layer (i.e. a model lithosphere). Although a useful analogue for the plate tectonic style of mantle convection that is peculiar to the Earth, as a starting point for an analysis of partial insulation this regime is a special limit. Indeed, to achieve this regime Lenardic *et al.* (2005) apply a viscoplastic yielding rheology that allows for both an active-lid mode of convection and for an internal mantle viscosity that is Newtonian and depends strongly on temperature. In more detail, subduction of the cold boundary layer (i.e. the analogue lithosphere) occurs where convective stresses exceed a critical yield stress, resulting in a localization of shear strains and the mechanical failure and overturning of the cold boundary layer and a large-scale flow. Because strain localization occurs where the effective viscosity is very low, the process of overturning of the cold boundary layer is effectively inviscid and thus most of the dissipation occurs in the fluid interior. In addition, because the

cold surface temperature of the model Earth is stirred into the underlying mantle, the time-averaged interior temperature is close to the mean of the two boundaries. In contrast, convection under the same dynamical conditions in a Newtonian fluid with a strongly temperature-dependent viscosity is typically in a 'stagnant-lid' regime. Flow in the form of intermittent drips (thermals) from the cold upper boundary occurs beneath a thick stagnant lid of relatively much more viscous fluid (see discussion in § 3). There is no large-scale overturning flow, and 'small-scale' thermals carry only a minor fraction of the temperature drop across the cold boundary layer, resulting in an internal temperature significantly higher than the mean of the boundaries. The reduced temperature difference to the hot boundary leads, in turn, a lower average basal heat flux. In addition, the formation of cold thermals involves the deformation of fluid that is about 10 times more viscous than the interior and thus most of the dissipation occurs within the cold boundary layer itself, causing the structure of the cold thermal boundary layer to be qualitatively different to the active-lid case.

Bearing in mind these essential differences between the active- and stagnant-lid regimes, the general question of the influence of partial insulation on variable viscosity convection (i.e. $\mu(T)_{max}/\mu(T)_{min} \gg 1$) in a Newtonian fluid remains an open one. In terms of laboratory experiments, published studies are largely limited to isoviscous or mildly temperature-dependent viscosity convection (Guillou & Jaupart 1993; Zhang & Libchaber 2000). The core of this study is a suite of laboratory experiments that explore partially to fully insulated convection in a high-Prandtl-number fluid with a strongly temperature-dependent viscosity. Preliminary results from this experimental suite were presented in the form of a Nusselt number versus insulation extent plot in Lenardic *et al.* (2005). That plot showed a peak in system heat transfer at an insulation extent of 0.2 of the full tank width. We significantly extend this work herein. In particular, we characterize and analyse the scale and vigour of overturning motions arising due to a partial lid, and investigate conditions in which such motions lead to local and global heat transfer maxima that are in excess of the classical no-lid value. Our analysis of the global heat transfer properties of these flows is based on a thermal network approach, as in Lenardic *et al.* (2005). However, the difference between the physics of (uninsulated) active versus stagnant-lid convection requires, and leads to, a new scaling theory. On the basis of our experimental results, this new scaling theory and a suite of three-dimensional numerical simulations that significantly extend our parameter space, we will argue that global heat transfer maxima are robust properties of these highly nonlinear systems and that they reflect well-defined minima in their global thermal resistance.

Our paper is organized in the following way. In §§ 2 and 3 laboratory experiments are presented in which we analyse the effect of the surface area of an insulating lid on the convection. A scaling analysis of the effect of an insulating lid on the heat flux carried by the flow is developed in § 4 and compared with laboratory measurements. In § 5, to test the generality of our results we expand the parameter space investigated by the laboratory experiments with a suite of three-dimensional numerical simulations. We conclude in § 6.

2. Experiments

2.1. *Experimental set-up and strategy*

Our experiments are conducted in the apparatus sketched in figure 1. The 31.3 cm × 31.3 cm × 7.5 cm high tank is constructed of glass insulated with polystyrene foam. The floor of the tank is an aluminium heat exchanger through which hot water is

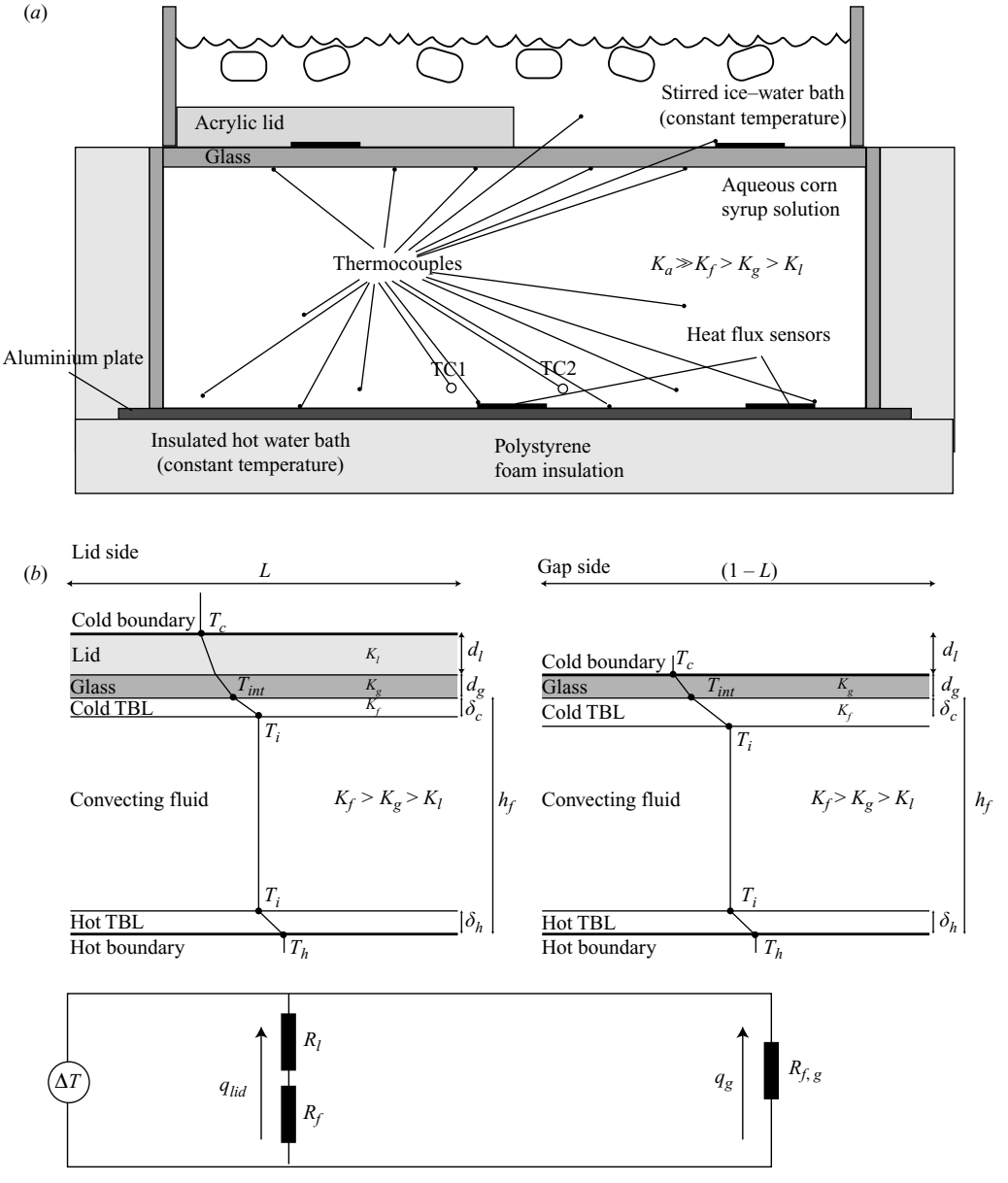

FIGURE 1. (*a*) Schematic diagram of our experimental setup. (*b*) Problem definition for the heat transfer analysis.

pumped at a high flow rate resulting in an isothermal basal temperature of ≈64.2°C at the base of the fluid layer. A glass heat exchanger in which there is a well-stirred ice–water bath forms a transparent upper isothermal cold boundary. The working fluid is an aqueous corn syrup solution, which is Newtonian and has a strongly temperature-dependent viscosity that is well represented by

$$\mu(T) = \mu_c \exp(-\gamma T), \tag{2.1}$$

Component	Physical property	Value (unit)
Glass	Thickness d_g	0.005 (m)
	Thermal conductivity K_g	0.81 ($\mathrm{W\,m^{-1}\,{}^{\circ}C^{-1}}$)
	Specific heat C_g	830 ($\mathrm{J\,kg^{-1}\,{}^{\circ}C^{-1}}$)
	Density ρ_g	2500 ($\mathrm{kg\,m^{-3}}$)
	Thermal expansion α_g	$9 \times 10^{-6}\,{}^{\circ}\mathrm{C^{-1}}$
	Thermal resistance d_g/K_g	0.0063 ($\mathrm{W\,{}^{\circ}C^{-1}}$)
Lid	Thickness d_g	0.012 (m)
	Thermal conductivity K_l	0.21 ($\mathrm{W\,m^{-1}\,{}^{\circ}C^{-1}}$)
	Specific heat C_l	1465 ($\mathrm{J\,kg^{-1}\,{}^{\circ}C^{-1}}$)
	Density ρ_l	1180 ($\mathrm{kg\,m^{-3}}$)
	Thermal expansion α_l	$9.2 \times 10^{-5}\,{}^{\circ}\mathrm{C^{-1}}$
	Thermal resistance d_l/K_l	0.057 ($\mathrm{W\,{}^{\circ}C^{-1}}$)
Fluid	Thickness h_f	0.0.075 (m)
	Thermal conductivity K_f	0.365 ($\mathrm{W\,m^{-1}\,{}^{\circ}C^{-1}}$)
	Specific heat C_f	2616 ($\mathrm{J\,kg^{-1}\,{}^{\circ}C^{-1}}$)
	Density ρ_f	1395 ($\mathrm{kg\,m^{-3}}$)
	Thermal expansion α_f	$5.61 \times 10^{-4}\,{}^{\circ}\mathrm{C^{-1}}$
	Reference viscosity μ_c	12 Pa·s
	Rheological temperature scale γ	$0.2 \pm 0.02\,{}^{\circ}\mathrm{C^{-1}}$

TABLE 1. Physical properties of the experimental system.

where μ_c is a reference viscosity, and the characteristic rheological temperature scale $\gamma = -\mathrm{d}\ln\mu/\mathrm{d}T$) (table 1).

A series of control experiments without an insulating lid are performed first. The qualitative structure and quantitative heat transfer properties of these flows are compared to previous studies of variable viscosity convection with isothermal upper and lower boundaries. In addition, the validity of the isothermal boundary conditions for all flows is verified. Next, a suite of experiments is performed in which a 1.2 cm thick block of acrylic is clamped to the floor of the cold bath as an insulating lid. The lid extends from the front to the back of the tank but has a width that we vary systematically. In 'partial lid' cases, where the lid does not extend the full width of the cold boundary, experiments are characterized by a laterally heterogeneous upper thermal boundary condition composed of a composite 'lid' and a 'gap' side. The heat transfer properties of each side are characterized in terms of their resistance to thermal conduction $d_{g,l}/K_{g,l}$, where d and K are an appropriate thickness and thermal conductivity, respectively, and the subscripts 'g' and 'l' refer to 'gap' and 'lid' sides of the tank, respectively. The physical properties and thermal resistances of the lid and gap sides are compared in table 1.

The structure and heat transfer properties of all flows are studied under statistically thermally steady-state conditions. The styles of convection are characterized quantitatively using a combination of time-lapse video, shadowgraph images and time series of temperature and heat flux at the floor, the roof and in the fluid interior. The interior fluid temperature and the temperature at the interface between the solid cold (and hot) boundary are determined from time-averaged measurements obtained from thermocouples distributed throughout the system. Local and average heat fluxes are obtained at the roof and floor of the tank using an array of Omega HFS-4 thermopile sensors, and from the temperature gradients across the solid boundaries, the physical properties of which are well known. Local heat fluxes obtained from both techniques are quantitatively identical. These measurements are also applied to verify

interfacial temperatures determined at the solid boundaries using thermocouples. Steady-state conditions are indicated by constant (and equal) average roof and floor heat fluxes, as well as statistically stationary time series of temperature in the interior.

2.2. *Dimensionless parameters and scaling*

Building on published investigations of Rayleigh–Bénard convection in variable viscosity fluids in the presence of rigid boundaries (e.g. Booker 1976; Richter, Nataf & Daly 1983; Zhang, Childress & Libchaber 1997; Manga & Weeraratne 1999; Jellinek, Lenardic & Manga 2002), we characterize our experimental system with six dimensionless parameters. The effective Rayleigh number for the composite system,

$$Ra_e = \rho^2 g \alpha \Delta T C H^3 / \mu(T_i) K, \tag{2.2}$$

which is essentially a ratio of the buoyancy force driving fluid motions, modulated by thermal diffusion, to the retarding viscous force arising due to the diffusion of momentum, is large in all experiments ($Ra > 5 \times 10^5$). Here, g is gravity, $\Delta T = T_h - T_c$ is the vertical temperature difference from the hot boundary to the cold bath and $\mu(T_i)$ is a viscosity based on the mean interior temperature of the fluid layer T_i. Here, subscripts h, c and m refer to the hot boundary, cold boundary and system mean, respectively. The effective layer depth

$$H = h + d_g + (d_l L) \tag{2.3}$$

includes the fluid layer height h, the thickness of the overlying glass d_g and the effective thickness of the insulating lid, which depends on the thickness of the lid d_l and the fractional areal extent of the lid L, defined below. An effective volumetric coefficient of thermal expansion, density, thermal conductivity and specific heat for the composite system are, respectively,

$$\alpha = (1/H)(\alpha_f h + \alpha_g d_g + \alpha_l d_l L), \tag{2.4}$$

$$\rho = (1/H)(\rho_f h + \rho_g d_g + \rho_l d_l L), \tag{2.5}$$

$$K = (1/H)(K_f h + K_g d_g + K_l d_l L) \tag{2.6}$$

and

$$C = (1/H)(C_f h + C_g d_g + C_l d_l L). \tag{2.7}$$

Here the subscripts f, g and l refer to 'fluid', 'gap' and 'lid', respectively. The aspect ratio of the system

$$A = w/h, \tag{2.8}$$

where w is the width of the tank, is fixed to be 4.2. The Prandtl number

$$Pr = \mu C / K \tag{2.9}$$

is a fluid property that indicates the ratio of time scale for the thermal diffusion of heat to the time scale for the viscous diffusion of momentum. In our experiments and numerical simulations Pr is sufficiently large ($Pr > 10^4$ in experiments and $Pr = \infty$ in numerical simulations) so that inertial forces have a negligible effect on the dynamics of flow (i.e. the Reynolds number, $Re < 0.1$ in the experiments and $Re = 0$ in the simulations). From (2.1), we characterize the magnitude of the temperature

dependence of the viscosity in terms of the parameter

$$\Lambda = \gamma \Delta T. \tag{2.10}$$

In our experimental system, γ is fixed and the total viscosity ratio across the fluid layer $\lambda_t = \mu_c/\mu_h$ is of order 10^5. In subsequent numerical simulations we vary Λ such that λ_t is in the range 10^0 to 10^6.

To characterize the influence of an additional insulating lid at the cold boundary we require two additional parameters. For an $\ell \times w$ rectangular lid, the lid surface area per unit surface area w^2 of the tank is

$$L = \ell/w. \tag{2.11}$$

Although the lids in our experiments are rectangular, different lid shapes are, in principle, possible for the same surface area implied by L. This is potentially an important consideration because the spatial configuration of variations in surface cooling will influence the planform of convection in the underlying fluid layer (Guillou & Jaupart 1993), which will influence the heat transfer properties of the flow. The rectangular shape of the lids in our experiments impose a fore-aft geometric symmetry on the flows. In subsequent numerical simulations we break this symmetry, and investigate its importance, with square lids characterized by the same L. Finally, we characterize the insulative properties of the lid with a Biot number

$$Bi = d_l K_g / d_g K_l, \tag{2.12}$$

which is the ratio of the thermal resistance of the insulating lid to conductive heat transfer to the thermal resistance of the glass forming the cold upper boundary. In the experiments Bi is fixed to be 9.3 and in our subsequent numerical simulations $Bi = \infty$, which has a quantitatively identical effect on the flow and simplifies the numerical treatment of the system.

In addition to these external parameters it will be useful to introduce a number of internal parameters derived from the experiments. The internal temperature of the fluid

$$\theta = (T_i - T_c)/(T_h - T_c), \tag{2.13}$$

where the subscript 'i' refers to the mean interior temperature. The horizontal difference between the glass–fluid interfacial temperatures at lid and gap sides is

$$\theta_h = \left(T_{int}^l - T_{int}^g\right)/(T_h - T_c). \tag{2.14}$$

Here, $T_{int}^{g,l}$ is measured at the top of the fluid layer at the interface between the fluid and the cold boundary on the 'gap' or 'lid' side of the tank. For comparison with previous work and to facilitate analysis of heat transfer from the hot boundary we introduce a basal Rayleigh number based on the depth and physical properties of the fluid layer, and the temperature drop from the hot boundary to the convecting interior $\Delta T_i = (T_h - T_i)$,

$$Ra_i = \rho_f^2 g \alpha \theta \Delta T_i C_f h^3 / \mu(T_m) K_f, \tag{2.15}$$

where $T_m = (T_h - T_c)/2$. For analysis of heat transfer to the cold boundary in the stagnant-lid regime where $\mu(T_{int}^{g,l})/\mu(T_i) > O(10^2)$ (Morris & Canright 1984; Manga *et al.* 2001; Thayalan *et al.* 2006) it will be useful also to introduce a Rayleigh number based on the rheological temperature scale γ,

$$Ra_\gamma = \rho_f^2 g \alpha C_f h^3 / \mu(T_m) \gamma K_f, \tag{2.16}$$

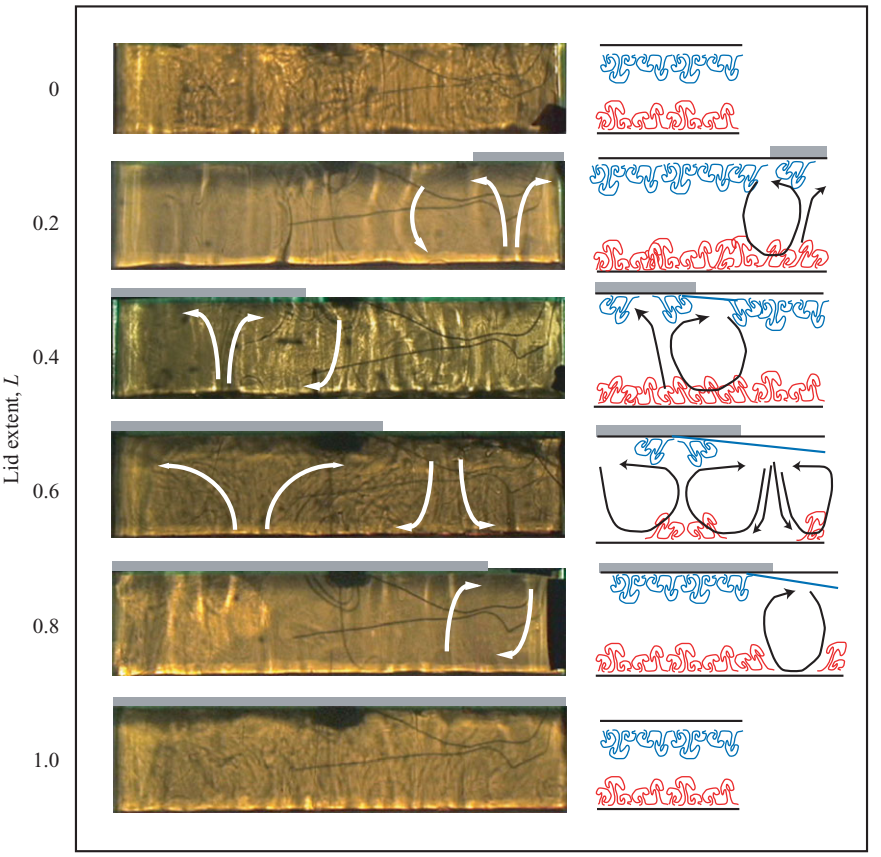

FIGURE 2. Regime diagram summarizing the influence of an insulating lid of extent L on the flow. The left panel shows shadowgraph images of typical experiments. The right panel shows sketches of the main components of each flow regime. Ascending (red) and descending (blue) thermals sketched in the right panel appear as time dependent, nearly vertical light (downwelling) and dark (upwelling) structures in the shadowgraphs. Arrows indicate the large-scale flow as determined from analyses of video data. Also shown are the relative thicknesses of the hot and cold thermal boundary layers (solid blue line). See figure 3(*b*) and the text for the experimental conditions.

where T_m is the mean of the boundary temperatures. Finally, a Rayleigh number based on the horizontal temperature difference at the top of the fluid layer $\Delta T_h = T_{int}^l - T_{int}^g$,

$$Ra_h = \rho_f^2 g \alpha \theta_h \Delta T_h C_f h^3 / \mu(T_i) K_f, \tag{2.17}$$

characterizes the vigour of convective motions driven by lateral variations in temperature related to the presence of a partial insulating lid.

3. Experimental results

3.1. *Flow regimes*

Analyses of time-lapse video, shadowgraphs and time series of temperature reveal three flow regimes, depending on the lid extent L, which are summarized in figure 2. For the control case, $L = 0$, the strong temperature dependence of the viscosity leads to large vertical viscosity variations in the cold thermal boundary layer

($\mu(T_c)/\mu(T_i) \sim O(10^5)$) and the flow is in the well-studied 'stagnant lid' regime (Booker 1976; Stengel, Oliver & Booker 1982; Richter *et al.* 1983; Christensen 1984; Ogawa, Schubert & Zebib 1991; Giannandrea & Christensen 1993; Moresi & Solomatov 1995, 1998; Solomatov, 1995; Solomatov & Moresi 1996, 2000; Trompert & Hansen 1998). In this regime, the flow is constructed of three layers (figure 2, right panel): thin gravitationally unstable conductive thermal boundary layers at the hot and cold boundaries underlie and overlie a well-mixed interior. The cold boundary layer is thicker than the hot boundary layer because the majority of its thickness is too viscous to take part in the flow (Davaille & Jaupart 1993). Convection is driven by the intermittent detachment of a thin rheological sublayer of cold fluid as discrete thermals or diapirs with transient tails (Weeraratne & Manga 1998; Jellinek *et al.* 2001) that carry only a fraction of the full temperature difference across the cold boundary layer and are around 10 times more viscous than the interior fluid. The interior temperature θ_i of the system is consequently higher than the mean of the hot and cold boundaries (i.e. $\theta_i > 0.5$) (figure 3*a*). In turn, because θ_i approaches θ_h, flow from the relatively thin hot boundary layer is an approximately isoviscous rising thermals (Weeraratne & Manga 1998; Jellinek & Manga 2004).

By contrast, for $L = 1$ the internal temperature is relatively higher because of the greater insulating effect of the additional lid. That is, the imposed plastic lid acts in much the same way as a stagnant lid but absorbs a greater fraction of the total temperature drop across the system because of a higher intrinsic thermal resistance (Sleep & Jellinek, 2008). The three-layer structure of the flow and the style of convection from the cold boundary is, however, broadly similar to the stagnant-lid regime with a key difference being that the cold thermal boundary layer is approximately isoviscous and approximately of the same thickness as the hot thermal boundary layer. That is, the structure of the flow for $L = 1$ is essentially symmetric whereas a defining characteristic of the flow for $L = 0$ is a broken symmetry in the vertical thermal structure of the flow (Solomatov 1995; Zhang *et al.* 1997).

The character of the flow in the presence of a partial lid is qualitatively different to the $L = 0$ and $L = 1$ cases. At the roof of the tank, the flow can be divided laterally into two regions. Far from the lid-gap boundary, the flow is similar to the $L = 0$ and $L = 1$ control experiments: Convection from beneath the lid and gap sides is in the form of intermittent thermals descending from uniformly thick thermal boundary layers. However, an important difference to the control experiments is that compared to the lid side the thermal boundary layer beneath the colder gap side is relatively thick and downwellings carry a larger temperature difference into the underlying fluid interior. Because the experiments are in steady state this variation in thickness is a response to horizontal variations in surface heat flux resulting from a combination of a partial insulating lid and an overlying isothermal cold bath. As a result, in the vicinity of the lid–gap boundary, there is a monotonic increase in thermal boundary layer thickness from the lid to the gap sides. The corresponding horizontal variations in heat flux lead, in turn, to a lateral temperature gradients (figure 3*a*, inset) that drive large-scale flows the character of which depends on L, the aspect ratio of the system and presumably also on the magnitude and character of the viscosity variations in the cold thermal boundary layer (cf. (2.1)). Thus, a major effect of imposing partial roof insulation on a stagnant-lid regime is to introduce additional lateral asymmetry to both the thermal and viscosity structures of the system.

In the shadowgraphs and accompanying sketches in figure 2, arrows determined from analyses of time-lapse video indicate that partial lid regimes are characterized by large-scale stirring, in addition to rising and sinking thermals. Qualitatively, all

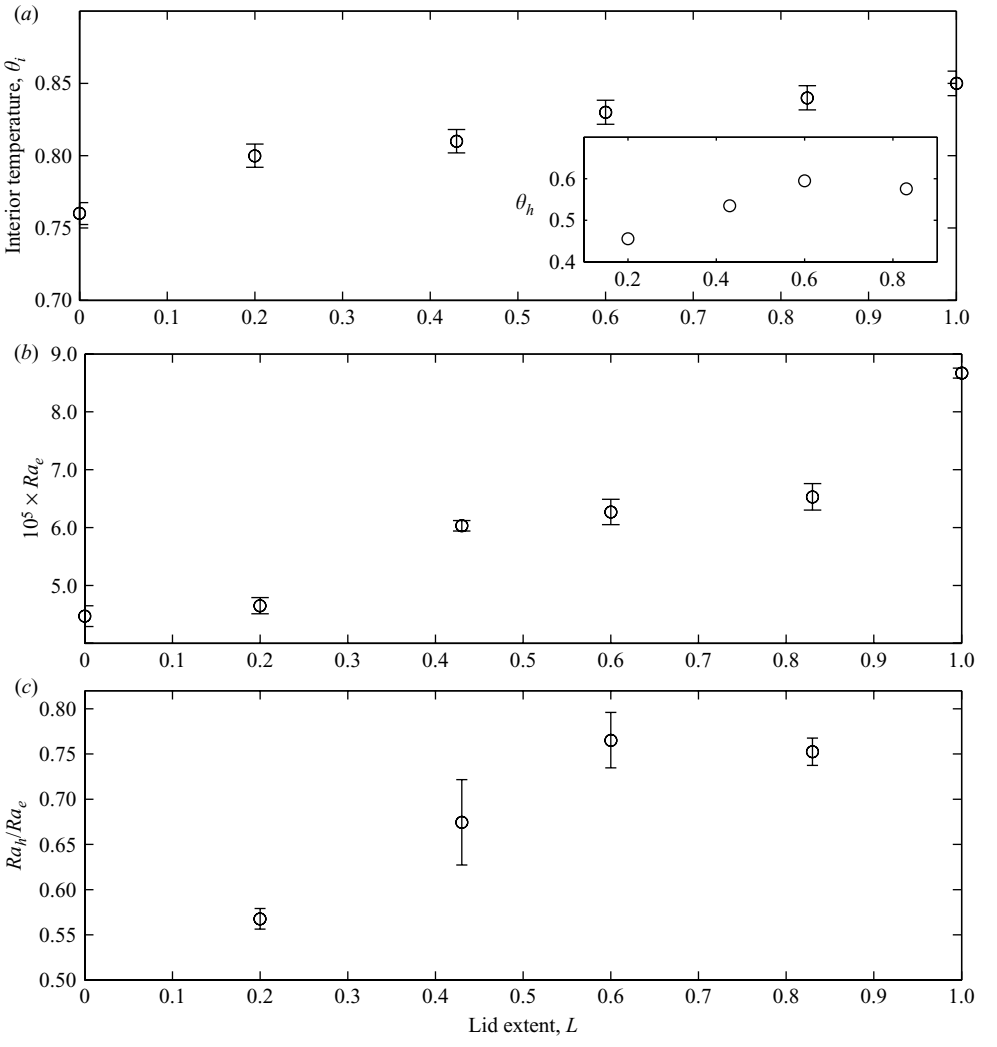

FIGURE 3. Plots showing (a) the mean internal temperature θ and (inset) the horizontal temperature difference at the cold boundary θ_h, (b) the Rayleigh number Ra_e and (c) the ratio Ra_h/Ra_e as a function of the fractional lid extent L. The ratio Ra_h/Ra_e indicates the vigour of overturning motions driven by lateral temperature gradients, in comparison to rising and sinking thermals. The internal fluid temperature $\theta \approx 0.76$ and is slightly higher than the $\theta \approx 0.7$ value obtained by Manga & Weeraratne (1999) for similar experimental conditions. This discrepancy occurs because the internal temperature is defined on the basis of the bath temperature rather than the temperature at the top of the fluid layer.

partial lid experiments are characterized by persistent unsteady upwellings into the base of the lid side, consistent with the isoviscous results of Guillou & Jaupart (1995) and also with the investigation of turbulent convection by Zhang & Libchaber (2000). The strength of the cold downwellings and the lateral extent and vigour of the large-scale flow is apparently governed by the extent of the lid L. In the 'short lid' case ($0 < L \leqslant 0.2$) the large-scale flow has a lateral extent that scales approximately with L. By contrast, in the 'long lid' case ($0.83 \leqslant L < 1$) overturning motions are restricted in horizontal extent to a region close to the width of the

gap and thus scale approximately as $(1 - L)$. In this regime the flow is separated laterally into approximately two parts: rising and sinking thermals beneath the lid and convection through a combination of thermals and overturning motions beneath the gap. At $L = 0.6$ the large-scale flow fills the full width of the tank and advects plume instabilities near the hot boundary laterally in a way analogous to the 'plume cluster' regime identified in the isoviscous experiments of Guillou & Jaupart (1995). The most complicated flow regime is the $L = 0.43$ case in which motions acting over a large range of length scales advect plume instabilities, particularly beneath the lid–gap boundary.

Quantitatively, In addition to imparting lateral temperature gradients that drive overturning motions (figure 3*a*, inset), a partial insulating lid raises the average internal temperature of the system roughly in proportion to L (figure 3*a*). This effect leads to a reduction in the average viscosity of the fluid, expressed, in part, through an increase in Ra_e in figure 3(*b*), as L is increased from 0 to 1. This effect demonstrably enhances the rate of rise (or descent) of hot (or cold) thermals, which is approximately proportional to $Ra_e^{1/3}$, as well as the rate at which large-scale motions stir the fluid interior. The vigour of the large-scale flow and the extent to which this flow governs the vertical heat transfer across the layer for a given L depends critically, however, on the magnitude of the driving lateral temperature variations imparted at the top of the fluid layer (figure 3*a*, inset). In figure 3(*c*) the ratio Ra_h/Ra_e, which indicates the relative driving forces for overturning motions and thermals, is maximized at $L = 0.6$, although the viscous resistance to flow is minimized for larger L. This result indicates an optimized interplay among the four main factors that govern the vigour of the large-scale stirring: the lid extent, the internal temperature, the rheology of the fluid and the magnitude of the lateral temperature variations imparted to the top of the convecting layer.

3.2. *Local dynamics of the hot thermal boundary layer*

Figure 4 shows time series of temperature from two thermocouple probes located within the hot thermal boundary layer, which are labelled as 'TC1' and 'TC2' in figure 1. The time series indicate temporal variations about the mean temperature. Also shown (figure 4, inset) are differenced data in which the high-frequency content of the signals associated with the formation of thermals is enhanced. All flows are unsteady. The $L = 0$ and $L = 1$ cases are characterized mostly by intermittent hot anomalies related to thermals. In the $L = 0$ case longer period cold thermals are also observed (Schaefer & Manga 2001; Robin *et al.* 2007). There is an additional long-period variation of the mean temperature that may reflect a weak overturning flow, consistent with Weeraratne & Manga (1999) who identify the emergence of a large-scale flow in addition to thermals at $Ra \sim O(10^5)$. An indication of the small strength of this flow and its relative unimportance to the vertical heat transfer across the layer is that the internal temperature is quantitatively consistent with a fully developed stagnant-lid regime (figure 3*a* and §4) in which the heat flux carried predominantly by rising and sinking thermals is independent of the layer depth (§§ 3.3 and 4.1).

In contrast, figure 5 shows that in partial lid experiments longer period hot structures associated with large-scale stirring occur in addition to short period hot thermals. The nature of the additional longer period harmonics, as well as the relative power distribution among these features vary with the lid extent. Spectra for the $L = 0.2$ and $L = 0.83$ cases are each characterized by power distributed

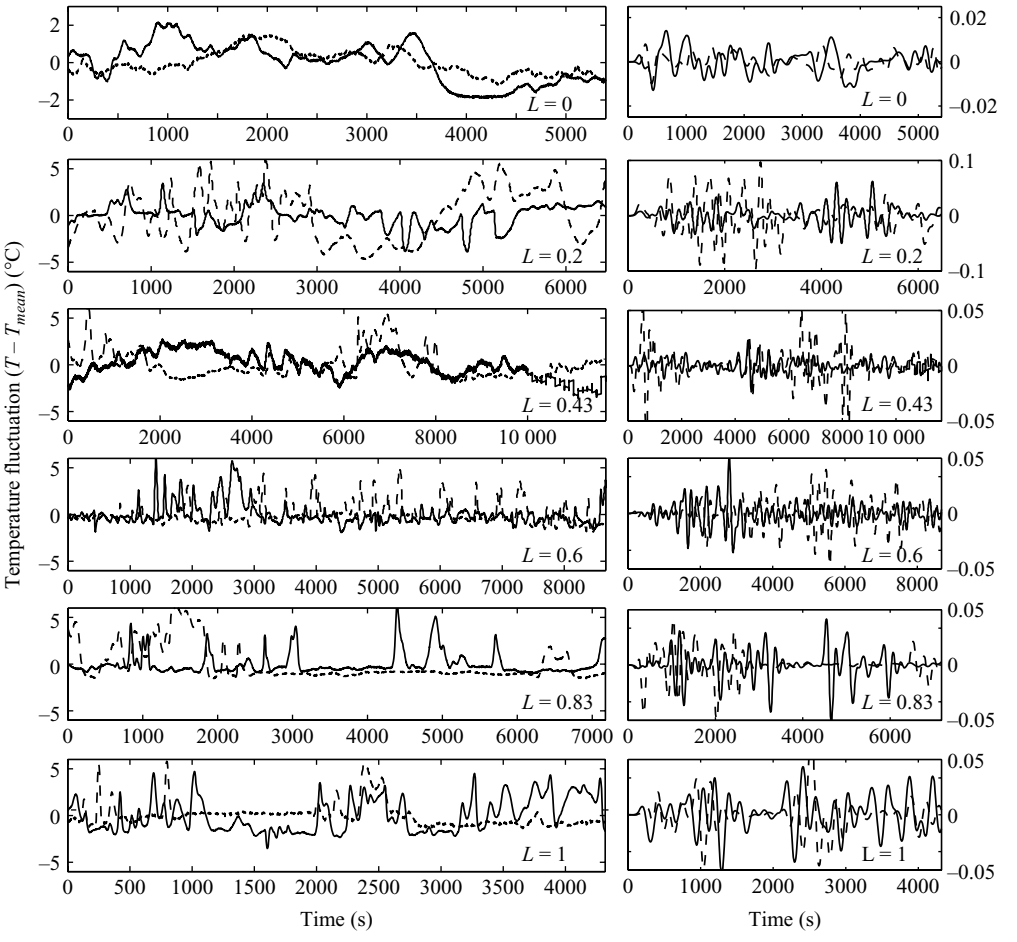

FIGURE 4. Plots showing time series of temperature variations about the mean temperature of the hot thermal boundary layer recorded by thermocouples 'TC1' (solid line) and 'TC2' (dashed line) (left panel). Also shown are the same data after it has been low pass filtered and differenced such that the contributions of thermals to the signal in each regime emerges more clearly (right panel).

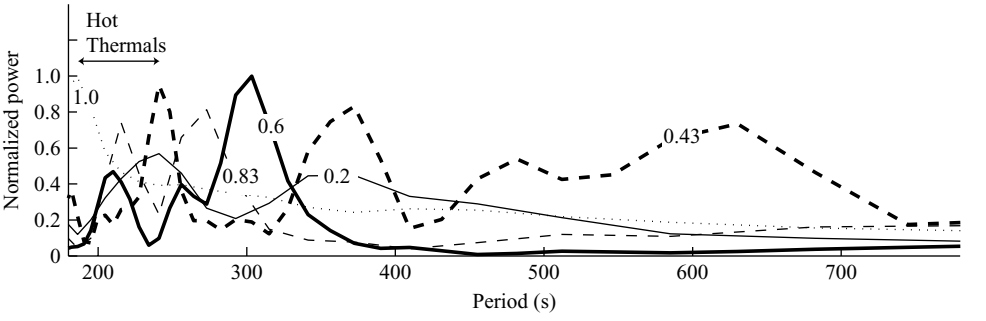

FIGURE 5. The power spectra for the time series of temperature for TC1 from figure 4 plotted as a function of lid extent L. Spectra shown are estimated with an adaptive multitaper method (see Appendix A).

approximately evenly between two periods corresponding to thermals and the largest scale overturning motion apparent in figure 2. The comparatively broad distribution of power at the longer periods for the $L = 0.2$ case may indicate that the large-scale flow is relatively more complicated. However, this result is influenced by the sensors not being ideally located to characterize this flow regime and should be interpreted cautiously. The $L = 0.6$ case is also characterized by two periods, although the long-period signal is concentrated over a narrower range of frequency bands, consistent with the quasi-steady tank-filling flow observed. In marked contrast, the $L = 0.43$ regime involves comparable power distributed over the most numerous as well as the longest periods. In particular, although a distinct period of thermal formation is observed, there is statistically significant power distributed broadly about two longer periods. This result is consistent with the observation that complicated unsteady motions occur over a range of time and length scales (§ 3.1 and figure 2).

3.3. *Rising thermals and lateral motions in the hot thermal boundary layer*

The results of numerous published studies of variable viscosity convection at high Ra and high Pr show that the formation of hot thermals is governed by the diffusive growth and intermittent detachment of the gravitationally unstable hot thermal boundary layer (e.g. Manga & Weeraratne 1999). This condition implies that the hot thermal boundary layer is on average critically thick and that heat transfer is governed by local processes and independent of the layer depth. If accurate, this picture implies that the period of thermal formation will be proportional to $Ra_e^{-2/3}$ (Howard 1964; Schaeffer & Manga 2001). Periods for hot thermal formation are identified at TC1 and TC2 in all experiments. In figure 6 we plot the average period from both locations as a function of L against $Ra_e^{-2/3}$ and find very good agreement with Howard's theory, consistent with the thermals observed in all experiments (figure 2).

The implication that heat transfer is independent of the layer depth in the vicinity of the sensors is surprising for the $L = 0.43$ and $L = 0.6$ and possibly $L = 0.83$ regimes because overturning motions interact with the hot boundary layer as well as nascent upwellings near both sensors. In particular, lateral motions advect hot fluid causing local variations in thermal boundary layer thickness and the downstream movement of nascent thermals (Jellinek, Gonnermann & Richards 2003; Gonnermann *et al.* 2004). A practical consequence of this interaction is that we can use the time for thermals to be advected between the sensors to estimate the average velocity of lateral motions within the hot boundary layer (e.g. Niemela *et al.* 2000). Quantitatively, we investigate whether the signal at TC2 is the same signal recorded at TC1, but shifted in time because hot convective instabilities are advected by the large-scale flow. A velocity is obtained from this lag time and the distance between the sensors. The methodology is outlined in detail in the Appendix. Figure 7 shows the estimated average horizontal velocity near the hot boundary normalized to a characteristic scale for the rise speed for thermals that is proportional to $(\kappa/H)Ra_e^{1/3}$ (cf. Jellinek *et al.* 2003). Whereas this velocity ratio is 0 for $L = 0$ and $L = 1$ it is maximized when $L = 0.6$, which is a regime characterized by the most intense tank-filling flow (figure 2), and minimized at $L = 0.83$. No reliable estimate was possible at $L = 0.2$ because of the position of the sensors relative to the location of the overturning flow (cf. § 3.2). From further comparison with figure 3(*c*), the magnitude of the increase in lateral velocity from $L = 0.43$ to a well-defined maximum at $L = 0.6$ is similar to the variation of the total driving force for large-scale flow Ra_h with L.

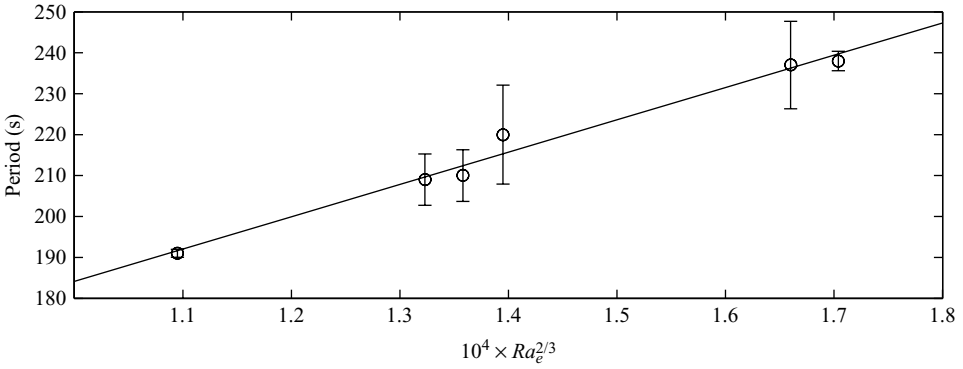

FIGURE 6. A comparison of the estimated periods for thermal formation and Howard's theory assuming heat transfer is independent of the layer depth.

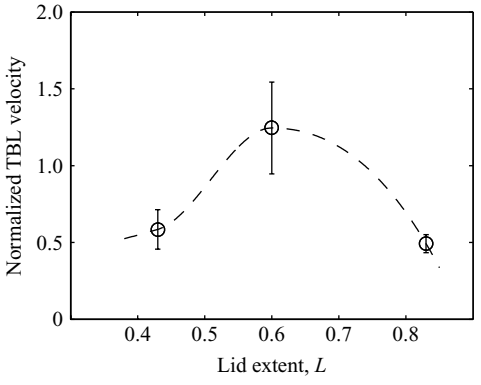

FIGURE 7. Variations in the horizontal flow velocity within the hot boundary layer, normalized to a scale for the rise velocity for hot thermals, as a function of lid extent L. Velocities are estimated using the technique outlined in Appendix A.

3.4. *Heat transfer*

Figure 8 shows a comparison of the measured average dimensionless heat flux through the gap side Q_{gap} and the measured average dimensionless global heat flux or Nusselt number Nu from the hot boundary as a function of lid extent. All heat fluxes are non-dimensionalized with the conductive heat flux across the system and then normalized to the average heat flux for the $L = 0$ case. Dotted lines indicate only the trend in the data, a scaling analysis for which is developed in §4. Two results are apparent. First, partial lid regimes exist where despite insulation at the cold boundary the local heat flux through the gap side and the average heat flux carried across the system *exceed* the $L = 0$ case. Second, peaks in Q_{gap} and Nu occur for different L: Whereas Nu is maximized for $L = 0.2$, Q_{gap} is maximized for the $L = 0.6$ case, which is characterized by the highest Ra_h and the most vigorous and extensive convective stirring. From inspection of figure 8 together with figures 2 and 7 it is clear that whereas Q_{gap} is governed by the rate of overturning, the average heat flux carried across the system Nu depends in a potentially complicated way on L for our working fluid.

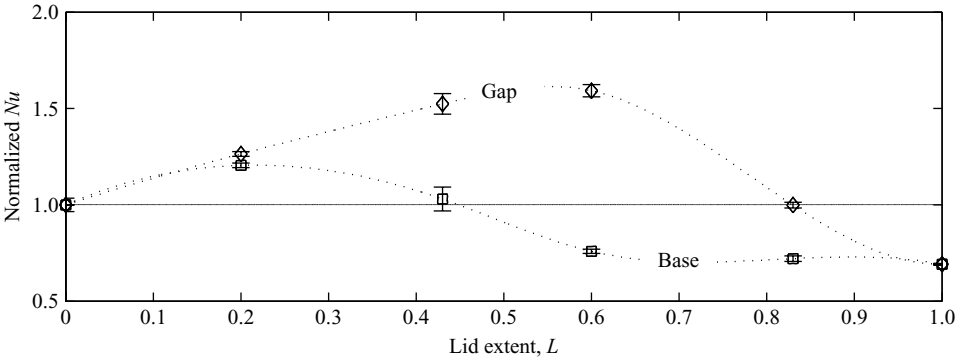

FIGURE 8. Measured variations of the average basal heat flux Nu (squares) and the heat flux through the gap side (diamonds) as a function of lid extent L. Dotted lines are spline fits to the data and are intended to show only the trend in the data.

3.5. *Summary*

Through varying an externally imposed control parameter, the insulation extent, we move our experimental system through a peak in its heat transfer properties while characterizing qualitative and quantitative changes in the flow regime. Our results show that there are two main mechanical effects of imposed partial insulation at the cold boundary that would otherwise be absent in a system convecting in the stagnant-lid regime. First, there is an increase in the internal temperature of the system that leads to a reduction in the average viscosity of the fluid layer. This effect enhances flow in all regimes. Second, for our working fluid partial insulation imparts a lateral asymmetry in the thermal structure of the flow that gives rise to lateral temperature and viscosity gradients in the cold thermal boundary layer, the magnitude and nature of which depend on L. These temperature gradients drive a large-scale flow that is governed by L but will probably be influenced by the magnitude of the temperature dependence of the viscosity Λ. In addition, the sensitive dependence of the flow regime on L suggests that variations in lid shape for a given L and Ra_e will also enter the problem. We explore effects related to lid shape, Λ and Ra_e with an additional limited suite of numerical simulations in § 5.

The most interesting consequence of partial insulation in our experiments is that the basal heat flux and the rate of overturn (or the local gap heat flux) have well-defined optimal values and that these values occur at different L. Whereas the flow velocity and gap heat flux are maximized where Ra_h is the largest and the overturning flow is the most vigorous, the average basal heat flux also depends strongly on the surface area of the gap side. In particular, there is a tradeoff between the rate at which large-scale overturning carries temperature variations away from the hot boundary and the surface area of the gap side through which most of this heat flux is delivered to the cold bath. The nature of this tradeoff is explored in § 4.

4. Scaling theory for the average basal heat flux

To build understanding of the global heat flux data in figure 9 we follow Lenardic *et al.* (2005) in spirit and model the system using a thermal network approach shown schematically in figure 1(*b*) (e.g. Incropera & DeWitt 1996). For a given flow regime the heat transfer across the gap or lid sides depends on the viscous resistance of the

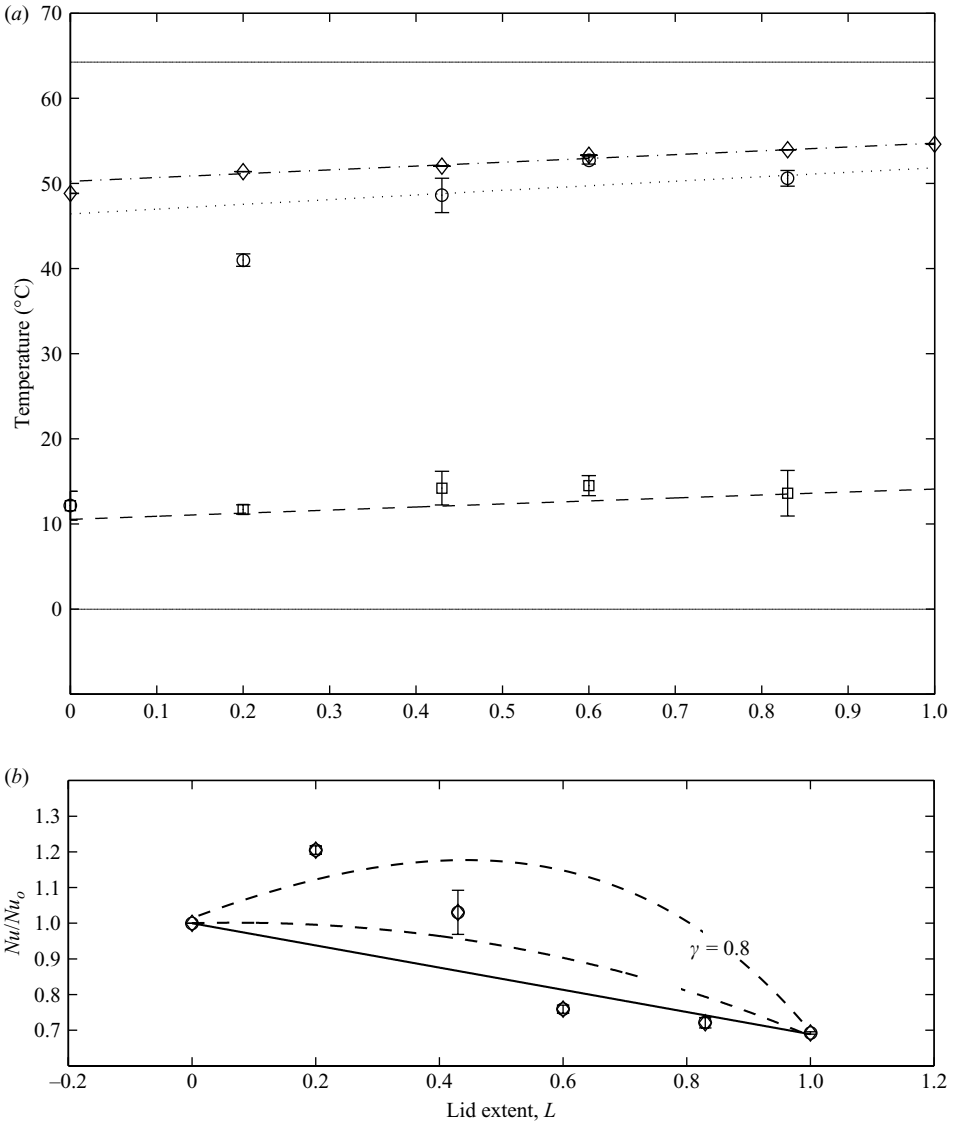

FIGURE 9. (*a*) Plot showing the temperature of the hot boundary and cold bath (solid black lines) and a comparison of theoretical predictions and data for the mean internal temperature (diamonds and dash-dot curve), the temperatures at the interface between the fluid and the cold boundary on the lid side (circles and dotted curve) and the interfacial temperature at the gap side (squares and dashed curve) as a function of lid extent L. (*b*) A comparison of the average basal heat flux as a function of L from figure 8 with predictions from the no-mixing (solid curve) and complete-mixing (dashed curve) theories outlined in § 4.3.

fluid to the motion of thermals and to large-scale stirring, as well as on the thermal resistance of the laminated cold boundary. The total heat transfer across the system is governed ultimately by the thermal coupling between the heat transfer paths to the lid and gap sides of the system, which varies in a complicated way with L. In more detail, because the two sides are coupled through the large-scale flow, variations in the heat transfer properties in one path can influence the other as well as the mean interior temperature of the system as a whole, which sets the average basal heat

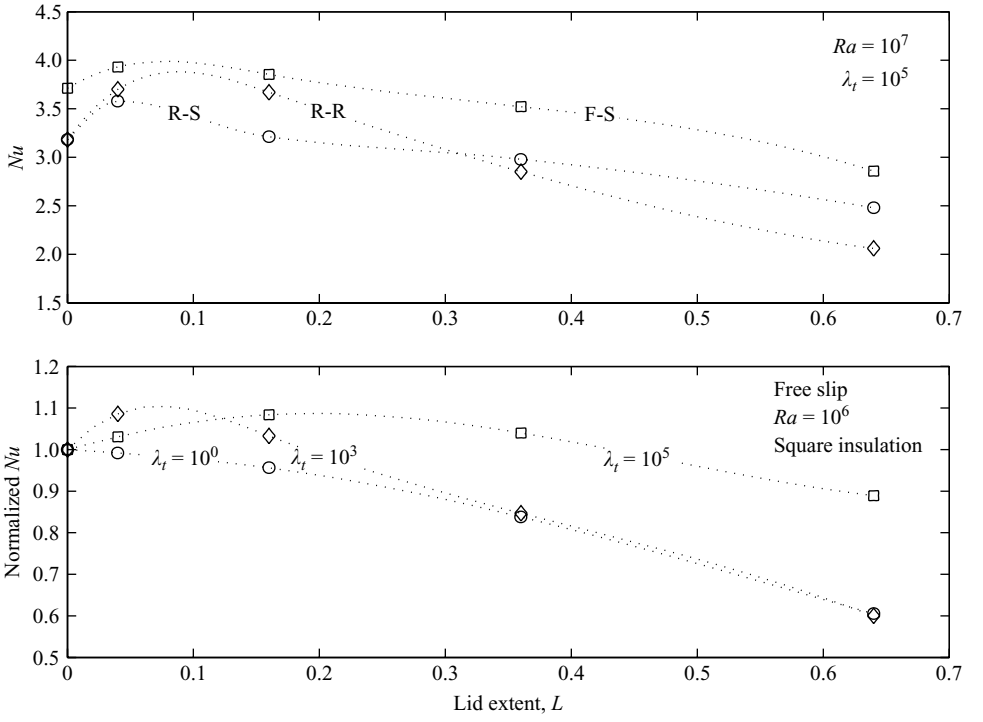

FIGURE 10. Calculations of the average basal heat flux from three-dimensional numerical simulations showing effects of the total viscosity variations in the system $\lambda_t = \mu_{cold}/\mu_{hot}$, lid shape and the mechanical boundary conditions in the system (rigid versus free-slip). R: 'rigid', F: 'free slip', S: 'square lid'. Comparison of the top and bottom plots provides a further indication of the influence of *Ra*. Dotted lines are spline fits to the data and are intended to show only the trend in the data.

flux. Bearing in mind this picture our analysis is constructed in the following way. We first characterize the heat transfer properties of flows with and without a lid. Expressions for the basal heat flux and internal temperatures for these endmembers are presented, in turn, and lead to predictions for the temperature at the interface between rigid cold boundary and underlying fluid. We are unable to find a satisfying theory for the variation of lateral temperature gradients at the top of the fluid layer and flow wavelength with *L*. Nevertheless, to investigate some general effects related to variable extents of thermal coupling with *L* we define the two limiting scenarios of no- and complete-mixing across the layer. Results of this analysis are compared with *Nu*–*L* data from figure 10.

4.1. *Full lid and lid-free cases*

We consider the two endmember model systems shown in figure 1(*b*). A fluid layer with depth h is convecting at high Rayleigh number and bounded uniformly at the top by a composite layer of glass with thickness d_g and an overlying insulating acrylic lid of thickness d_l. We assume that the system is convecting under thermally steady-state conditions. At high *Ra* the solid boundaries forming the lid and gap sides are each underlain by thin conductive thermal boundary layers with approximately uniform time-averaged thicknesses δ_c^l and δ_c^g, respectively, defined below. The cold

bath temperature T_c and the hot boundary temperature T_h are fixed. The mean interior temperature T_i depends on the conductive heat transfer across a cold thermal boundary layer, the glass and lid, respectively.

In the presence of a lid the dimensionless average roof heat flux or Nusselt number is

$$Nu_l = \left(\frac{HU_l}{K_f}\right)\left(\frac{T_{i,l} - T_c}{T_h - T_c}\right). \tag{4.1}$$

Here, the subscript l refers to 'lid side', and the heat transfer coefficient governing conduction across the composite cold boundary is given by the sum of the thermal resistance of each layer in series:

$$U_l = \left[\delta_c^l/K_f + d_g/K_g + d_l/LK_l\right]^{-1}, \tag{4.2}$$

where K_f, K_g and K_l are the thermal conductivities of the syrup, glass and lid, respectively. The average insulating effect of the lid on the system is assumed to scale with L such that the thermal resistance of the full thickness of the lid occurs where $L = 1$ and the no-lid case is recovered where $L = 0$. From examination of (4.1) and (4.2), Nu_l depends on T_i and the cold boundary layer thickness $\delta_{c,l}$ for which additional expressions are required.

Conservation of heat demands that the surface and basal heat fluxes balance. At high Ra_i the non-dimensional basal heat flux can be expressed as

$$Nu_l = a(Ra_{i,l}/Ra_{cr})^{\beta}, \tag{4.3}$$

where the critical Rayleigh number $Ra_{cr} = 1000$. Assuming Howard's theory applies on average, as suggested by our experiments (cf. §§ 3.1 and 3.2), heat transfer is independent of the layer depth and the power law exponent $\beta = 1/3$. The geometric constant $a = 0.23$.

Under steady-state conditions and assuming that convection from the base of the lid is approximately isoviscous, consistent with our results (and expectations for large-Bi regimes) the full thickness of the cold boundary layer scales as h_f/Nu_l and is given by (Solomatov 1995)

$$\delta_{c,l} \sim h_f {Ra_{i,l}}^{-\beta}. \tag{4.4}$$

Equating (4.1) and (4.3) leads, in turn, to an implicit expression for the dimensional internal temperature

$$a\left(\frac{\rho^2 Cg\alpha(T_h - T_{i,l})H^3}{Ra_c\mu_o \exp(-\Lambda T_m/\Delta T)K}\right)^{\beta} = \left(\frac{HU_l}{K_f}\right)\left(\frac{T_{i,l} - T_c}{T_h - T_c}\right). \tag{4.5}$$

Solving for $T_{i,l}$ numerically and equating the heat flux across the cold thermal boundary layer with the surface heat flux out of the system provides an additional useful result, which is the temperature at the interface between the rigid cold boundary and convecting interior is

$$T_{int,l} = T_{i,l} - \left(\frac{U_l\delta_{c,l}}{K_f}\right)(T_{i,l} - T_c). \tag{4.6}$$

Turning to the lid-free case the dimensionless heat flux at the surface of the system

$$Nu_g = \left(\frac{HU_g}{K_f}\right)\left(\frac{T_{i,g} - T_c}{T_h - T_c}\right), \tag{4.7}$$

Here, the subscript g refers to 'gap side' and, following from (4.2), the heat transfer coefficient is

$$U_g = \left[\delta_c^g / K_f + d_g / K_g\right]^{-1}. \tag{4.8}$$

If convection is taken to be in the stagnant-lid regime (i.e. $\mu(T_{int,g})/\mu(T_{i,g}) \geqslant O(10^2)$) (Thayalan *et al.* 2006) the full thickness of the the cold thermal boundary layer is expected to scale as (Morris & Canright 1984; Solomatov 1995; Manga *et al.* 2001)

$$\delta_c^g \sim \left(h_f / \Lambda^{1+\beta}\right) \mathrm{Ra}_\gamma^{-\beta}. \tag{4.9}$$

Balancing the surface and basal heat fluxes on the gap side

$$Nu_g = b(Ra_{i,g}/Ra_c)^\beta \tag{4.10}$$

leads to an expression for the dimensional interior temperature

$$b\left(\frac{\rho g \alpha (T_h - T_{i,g}) H^3}{\mu_o \exp(-\Lambda T_m/\Delta T)\kappa}\right)^\beta = \left(\frac{H U_g}{K_f}\right)\left(\frac{T_{i,g} - T_c}{T_h - T_c}\right), \tag{4.11}$$

where $\beta = 1/3$ and the constant $b = 0.12$. As before, applying T_i and equating the heat flux across the cold thermal boundary layer with the surface heat flux leads to the temperature at the interface between the rigid cold boundary and convecting fluid

$$T_{int,g} = T_{i,g} - \left(\frac{U_g \delta_{c,l}}{K_f}\right)\left(T_{i,g} - T_c\right). \tag{4.12}$$

4.2. *Partial lid case*

In the partial lid case the average basal heat flux depends on the surface area weighted contributions of the heat fluxes through the lid and gap sides as well as the resulting flow in the interior. Under steady-state conditions the areally-weighted dimensionless basal heat flux for the system as a function of L is

$$Nu = Nu_l(L) + Nu_g(1 - L). \tag{4.13}$$

A useful feature of (4.13) is that the competing influences of the thermal resistance of the system and surface area of the lid are apparent. In particular, the average basal heat flux is governed by an explicit competition between the effect of a partial lid on the internal temperature and thus viscosity and, by inference, the average flow velocity in the system, and the surface area through which heat can be transferred to the cold bath.

An appropriate choice of internal temperature for the viscosity requires discussion because it depends on the nature and extent of thermal mixing between the lid and gap sides, which are not accounted for in the theory. From figures 2 and 5 it is clear that flows driven by the lateral temperature gradients at the top of the fluid layer have a dominant wavelength that varies between the widths of the lid, gap and tank and thus this coupling is not straightforward, in detail. However, the regime diagram in figure 2 suggests two endmember situations. For experiments in which flows beneath the lid and the gap sides are essentially decoupled from one another (i.e. the 'no-mixing' case) we take the viscosity for each heat transfer path to be based on the mean temperature of the boundaries. The average basal heat flux is then a linear combination of the two sides. In contrast, for experiments characterized by a tank-filling flow and thorough thermal mixing (i.e. the 'complete mixing' case) we take the viscosity for the gap side to be based on the horizontally averaged value of

the whole convecting interior. In this case the average basal heat flux depends on a nonlinear coupling of the heat transfer paths through the lid and gap sides through the exponential temperature dependence of the viscosity (cf. (2.1)). An obvious limitation of this approach is that it is *ad hoc* and there is no account for variations in the mechanics and structure of the large-scale flow or the thermal boundary layers as a function of lid extent L.

4.3. *Comparison to experiments*

Theoretical and experimental results for the interior and interfacial temperatures at the lid and gap sides as a function of L are shown in figure 9 along with the corresponding variation of basal heat flux. In figure 9(a) measurements of the average internal temperature and the interfacial temperatures at the gap and lid sides are well explained by the theory for $L = 0$ and $L > 0.2$. The theory overpredicts the interfacial temperature at the lid side at $L = 0.2$. From examination of the flow regimes in figure 2 the mismatch at $L = 0.2$ is not surprising because the theory does not account for the observed large lateral variation in cold boundary layer thickness, which occurs over the full lid extent in this regime. The good agreement for larger L regimes is probably related to such variations in boundary layer thickness occurring over horizontal length scales that are small in comparison to the lid extent. That is, the assumption of an average thermal boundary layer thickness that was developed for a homogeneous thermal boundary condition and given by (4.4) is better justified for $L > 0.2$.

The two theories for the average basal heat flux are compared with heat flux measurements in figure 9(b). The no-mixing theory predicts a linear decline in heat flux with L, consistent with data for $0.6 \leqslant L < 1$. In contrast, the complete-mixing theory predicts a broad maximum centred around $L = 0.2$, qualitatively consistent in location in Nu–L parameter space with our measurements. However, the amplitude of the maximum is negligibly larger than the $L = 0$ case, which is much lower than the basal heat flux that we measure experimentally. Moreover, the only way to recover a comparable heat flux maximum with this theory is to increase γ by almost a factor of 4 (i.e. $\gamma = 0.8$), which is both inconsistent with our measured viscosity law and predicts the heat flux to be maximized at $L \approx 0.5$, which is not observed.

In summary, the theory captures some but not all of the key physics governing the heat transfer across the system. The predicted occurrence of a heat flux maximum at $L = 0.2$ highlights a tradeoff between lid surface area and flow velocity similar to that identified by Lenardic *et al.* (2005) for active-lid convection. The poor explanation of the heat flux amplitude at $L = 0.2$, and the particularly large overestimate of the value for the well-stirred $L = 0.6$ regime suggest that the nature of the lateral temperature gradients at the top of the fluid layer and the structure of resulting large-scale flow are probably equally important properties governing the heat transfer properties of these flows. A final remark is that the excellent theoretical agreement found for active-lid convection in Lenardic *et al.* (2005) supports this speculation. Because of the two-dimensional constant aspect ratio computational domain, as well as the nature of convection driven by yielding in a viscoplastic mantle, the geometric structure of the flows in Lenardic *et al.* (2005) is approximately fixed over the full range of parameter space investigated. In particular, an important difference to our experiments is that increasing L in Lenardic *et al.* (2005) leads to an enhanced rate of stirring without altering the intrinsic structure and wavelength of the overturning motions.

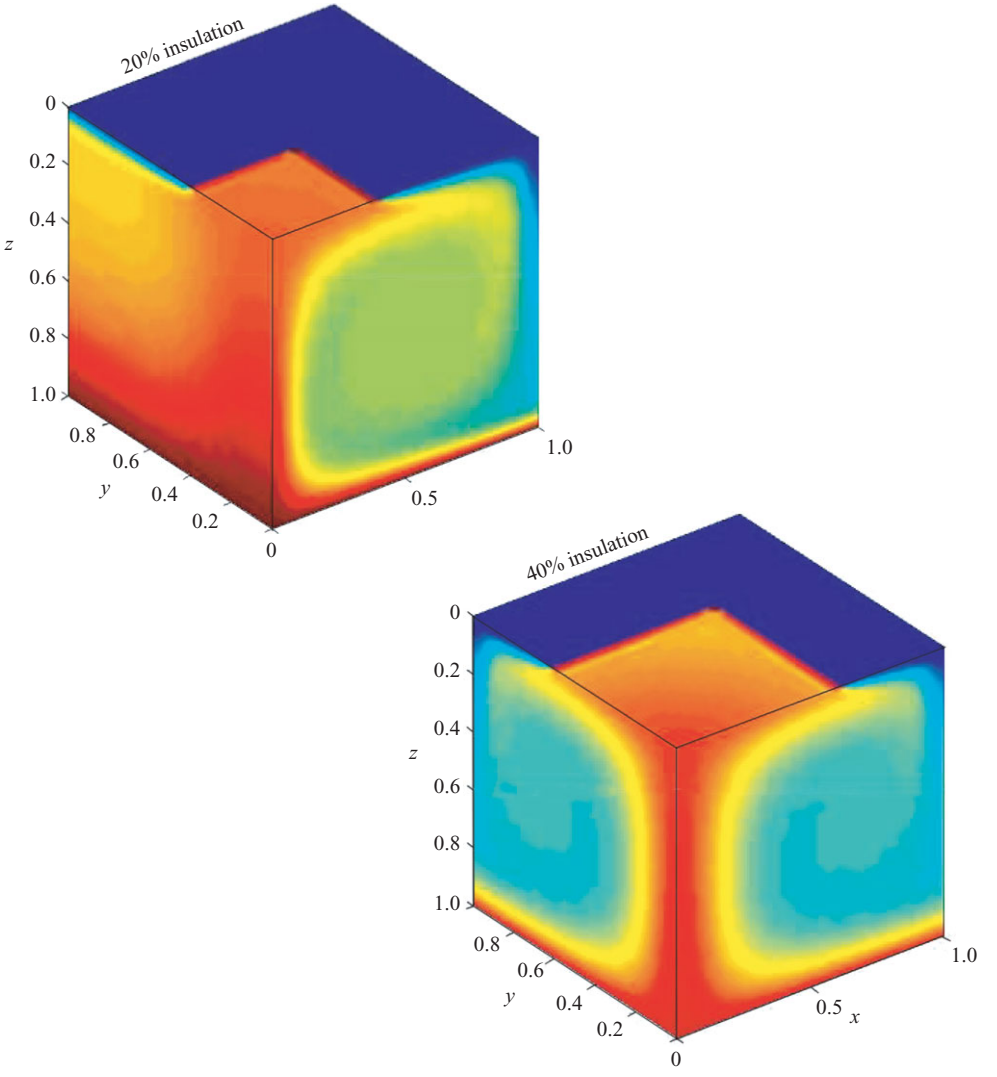

FIGURE 11. Snapshots from numerical simulations under statistically steady-state conditions showing the effect of the extent of a square lid on the planform of convective motions. Whereas quasi-two-dimensional rolls are observed for a lid covering 20 % of the top surface (i.e. $L = 0.2$), three-dimensional square cells emerge when the lid is increased to 40 % of the top surface area (i.e. $L = 0.4$). $Ra = 1 \times 10^6$.

5. Numerical simulations

The results from our laboratory experiments and scaling analyses show that partial insulation of a cold boundary can enhance the steady-state heat transfer properties of stagnant-lid convection in our working fluid. More generally, the magnitude of this effect depends on the rate and style of stirring, which depends on L and Ra_h, but is expected also to be a complicated function of Ra_e, Λ and lid shape. Whereas the lid shape for a given L influences the nature of the lateral temperature gradients and the wavelength of the large-scale overturning flow, Ra_e and Λ govern the thicknesses

of the hot and cold thermal boundary layers (cf. (4.5) and (4.10)), thereby setting the smallest scale of motion in the flow. To build some understanding of these effects we carry out a modest suite of numerical simulations with two motivations, which are to broaden the Ra_e–Λ parameter space explored and to investigate the effect of a different lid shape for the same areal extent L. Our aim is to investigate the sensitivity of the existence, shape and magnitude of maxima in Nu–L curves to these control parameters. As with the experiments we consider only those cases in which the lateral dimensions of the lid are much greater than the thickness of an unstable cold thermal boundary layer.

5.1. *Model formulation*

Numerical simulations using the serial CITCOM finite element code solve the equations of infinite Prandtl number thermal convection within a $1 \times 1 \times 1$ cubic modelling domain (Moresi & Solomatov 1995). Practical limitations related to computational resources lead us to not investigate larger aspect ratio domains at this time (subsequent to the undertaking of this study, a parallel version of the code has become available, as have greater computing resources at our respective institutions, and future work will explore larger aspect ratio domains). The accuracy of the code was tested against standard benchmark solutions (Blackenbach *et al.* 1989). Extensive convergence testing was also performed to assure that simulations are well resolved.

The non-dimensional system of equations solved are given by

$$\partial_m \boldsymbol{u}_m = 0 \tag{5.1}$$

$$\partial_n [2\mu(T)\epsilon_{mn}] = \partial_m p + Ra_e T \boldsymbol{k} \tag{5.2}$$

$$\partial_t T + \boldsymbol{u}_m \partial_m T = \partial_m^2 T \tag{5.3}$$

$$\rho = [1 - \alpha(T - T_0)] \tag{5.4}$$

where for convenience $Ra_e = \rho_0 g \alpha \Delta T D^3 / \mu(T_h)\kappa$ and $\boldsymbol{u}_i$ is the velocity vector, ϵ_{mn} is the rate of strain tensor, p is pressure and $\boldsymbol{k}$ is the vertical unit vector. Equations (5.1)–(5.3) are balance equations indicating conservation of mass, momentum and energy assuming no frictional or internal heating. Equation (5.4) is the linearized equation of state.

The system base was set to a constant non-dimensional temperature value of unity. The upper thermal boundary condition was laterally variable to mimic the effects of an insulating lid. In the lid regions the vertical heat flux was fixed to a value of zero (perfect insulation, $Bi = \infty$). We note that over a large number of simulation variations in Nu–L are only weakly dependent on the thermal resistance of the lid if $Bi \geqslant O(10)$. Consequently, we fix $Bi \rightarrow \infty$ for all simulations to simplify the numerical implementation of this effect and conduct simulations under Bi conditions comparable to our experiments. In lid-free regions the surface thermal boundary condition is set to a constant non-dimensional temperature value of zero. Variable mechanical boundary conditions at the system surface and base were explored as will be discussed. Side boundary conditions are free slip for all cases.

Simulations are run to to a statistically steady state determined by monitoring time series of Nu and and the r.m.s. velocity from each simulation. Simulation time series are averaged after the initial start up phase using variable averaging windows. A simulation is considered to enter a statistically steady state when averages determined from increasing time duration windows differed by less than 2 %–3 %.

5.2. *Numerical results*

Figure 10 shows the effect of changing the shape of the lid for a given L from rectangular, as for our experiments, to square. We also compare results for no- and free-slip boundaries. Dotted lines again show only the trend in the data. Figure 10(a) shows that the qualitative influence of a partial lid on the average basal heat flux carried by the flow Nu remains unchanged. However, quantitative differences emerge. In particular, for identical conditions the amplitudes of heat flux peaks are greater in the presence of free-slip boundaries than no-slip boundaries, which is expected as a result of the reduced viscous resistance to flow. Furthermore, a square rather than rectangular lid causes heat flux peaks to shift towards smaller L and to sharpen. Although the heat flux is controlled predominantly by the lid surface area, it is clear that lid shape and, by inference the structure of the longest wavelength motions, influences the conditions for which Nu is maximized.

Figure 10(b) shows results from a series of simulations in which we fix $Ra_e = 10^6$ and vary the magnitude of the temperature dependence of the viscosity Λ such that the corresponding total viscosity ratio across the system λ_t is in the range of 10^0–10^5. Simulations in which $\lambda_t = 10^5$ are under conditions comparable to our experiments and give Nu –L results that are quantitatively similar to those shown in figure 9. Decreasing λ_t, however, causes the peak in the heat flux curve to become increasingly narrow and also to shift towards smaller L. At $\lambda_t = 1$, the peak in the heat flux curve disappears entirely and Nu is a monotonically declining function of L. As with the laboratory experiments, the peak in r.m.s. velocity occurs at larger values of L than the peak in heat flux. For the isoviscous case the r.m.s. velocity is a weak function of L over the L range explored. Comparison of the two plots in figure 10 shows that increasing Ra_e shifts peaks in Nu–L curves to lower L and causes them to narrow in much the same way as observed with decreasing λ_t.

6. Concluding remarks

Our results support a number of general conclusions about the influence of a partial insulating lid on stagnant-lid convection at high Ra_e. Consistent with the analysis of active-lid convection by Lenardic *et al.* (2005) we find that the presence of an insulating lid leads to a higher internal temperature, a reduced interior viscosity and, in turn, to a more vigorous flow. Partial insulation introduces additional lateral temperature- and viscosity-gradients near the cold boundary that drive a large-scale overturning flow with a structure and wavelength that depends on the lid extent and shape. The most remarkable consequence of partial insulation is that the combined effects of an increased internal temperature and a lateral asymmetry in the thermal structure of the flow lead to distinct optimal values for the rate of overturn, the local gap heat flux and the global average basal heat flux. In addition, whereas flow velocities and gap heat fluxes are maximized where lateral temperature gradients are greatest, the global heat flux carried from the hot boundary across the system depends crucially on a tradeoff with the gap surface area, and thus occurs at different values for the lid extent L. Depending on the magnitude of the temperature dependence of the viscosity Λ, the optimal global heat flux can significantly exceed that carried by uninsulated stagnant-lid convection.

In more detail, with the exception of isoviscous flows ($\Lambda = 0$) a well-defined maximum in the basal heat flux Nu occurs for all Ra_e–Λ conditions investigated. The occurrence of such a maximum is insensitive to the mechanical boundary conditions applied and is not strongly influenced by lid shape. The magnitude and location of

this peak in Nu–L parameter space, however, depends in a complicated way on the lid surface area and on the strength and wavelength of the overturning motions. Whereas the rate of stirring for a given L is governed primarily by Λ through the nonlinear coupling of internal temperature to viscosity the structure and ultimately the heat transfer properties of the large-scale flow depend on the lid extent and shape and are almost certainly influenced by the aspect ratio of the system and the depth of the convecting layer. In our experiments, for example, dramatic variations in flow regime occur as L is varied (figures 2 and 5). In our experiments there is a transition from flow at the scale of the lid extent where $L = 0.2$ and Nu is maximized, to flow at the scale of the tank at $L = 0.6$ where the local gap heat flux is maximized, to flow at the scale of the gap at $L = 0.83$, where Nu is less than the uninsulated case. The effect of lid shape may be equally large. Figure 11 shows visualizations from simulations with square lids corresponding to $L = 0.2$ and $L = 0.4$ (all other conditions are identical between the calculations). The unsteady two-dimensional roll pattern apparent in the small surface area case evolves to a time-dependent three-dimensional square cell pattern when a larger lid is applied. In addition, our numerical simulations show that for a given Ra_e where rectangular lids are replaced with square lids a qualitative change in the largest-scale structure of the flow preserves the magnitude of the peak in heat flux, but causes it to shift to larger L.

We have two final comments. First, the link between the structure of the flow and the location of global heat transfer maxima in Nu–L parameter space is a key issue and remains an open problem. Second, our results combined with the active-lid study of Lenardic *et al.* (2005) suggest that a maximum in the basal heat flux is a fundamental property of partially insulated active- and stagnant-lid convecting systems. Moreover, it may be argued more generally on the basis of these robust features that these classes of convection problem are novel examples highly nonlinear systems with a well-defined minima in their global thermal resistance.

We thank N. H. Sleep, M. Manga and R. W. Griffiths for discussions and comments as well as R.-B. Lenardic for support. We are grateful particularly for thorough comments from several anonymous reviewers that improved this paper significantly. M. Wenzel provided crucial help with some of the experiments and drafted an earlier version of figure 1. This work was supported by funding from NSERC and the Canadian Institute For Advanced Research to AMJ, by NSF CAREER Grant EAR-0448871 to AL and by NSF EAR 0439766 to M. Manga.

Appendix. Power spectral estimation and the horizontal velocity in the hot thermal boundary layer

Power spectra from the data shown in figure 4 are estimated using both an adaptive Thompson multitaper algorithm (Thompson 1982; Park, Lindberg & Vernon 1987) and the method of Welch (1967). Periods for hot thermal formation at TC1 and TC2 are estimated from both techniques are compared in figure 13 and are quantitatively similar. Characteristic periods identified with spectral analysis are further verified from the periodic form of the autocorrealtion functions for the time series evaluated at large time lags (Lathi 1965; Manga & Weeraratne 1999) and, where possible, from visual inspection of the time series. To obtain a velocity for the $L = 0.43$, 0.6 and 0.83 regimes we hypothesize that the period of hot thermal formation observed at the upstream and downstream sensors are the same but shifted in time. We analyse the time shift between the signals and estimate a velocity from the measured distance between the

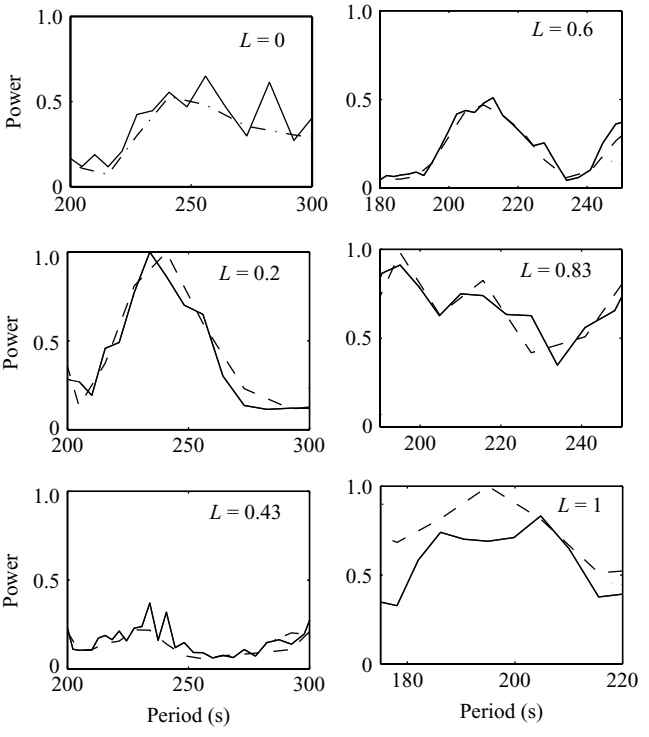

FIGURE 12. Spectral estimates for the periods of hot thermal formation determined using the Welch (solid line) and adaptive multitaper (dashed line) methods as a function of lid extent L.

sensors. To verify that the period of hot thermal formation at TC1 can be resolved at TC2 we cross-correlate the time series for TC2 with a synthetic monochromatic sinusoid with the measured period of hot thermal formation. Conceptually, we adopt the following approach. We define the average cross-correlation coefficient as the inner product of the synthetic sinusoidal signal $s(t)$ and the original time series $f(t)$

$$\varphi_{xy}(\tau) = \frac{1}{T}\int_{-\infty}^{\infty} f(t)s(t-\tau)\,\mathrm{d}\tau, \tag{A 1}$$

where T is the temporal length of $f(t)$ and τ is the time lag between the signals. If the $f(t)$ contains a component of the same period as $s(t)$, then $\varphi_{xy}(\tau)$ will be a periodic function with the same period as $s(t)$. In the alternative endmember situation that $s(t)$ and $f(t)$ are orthogonal, $\varphi_{xy}(\tau)$ will vanish. However, the power spectra in figure 5 show that whereas most power is primarily concentrated in two characteristic periods associated with the flow, there is non-negligible power distributed over a large range of frequency bands due to noise. Consequently, $\varphi_{xy}(\tau)$ will never vanish but can be characterized with a lower limit or 'noise floor' for each experiment that we estimate partly through the results of this test.

To determine the time shift between the time series we perform and compare two operations. First, we calculate discrete cross-correlations of the full time series from TC1 and TC2, as is done in studies of turbulent flows (e.g. Niemala 2000). Time lags associated with short period features such as thermals are shown in figure 14 as a function of L. To improve our estimates of these time lags we Fourier transform the cross-correlation function and obtain the complex cross-spectral density $\Phi_{xy}(\mathrm{i}\omega)$ where

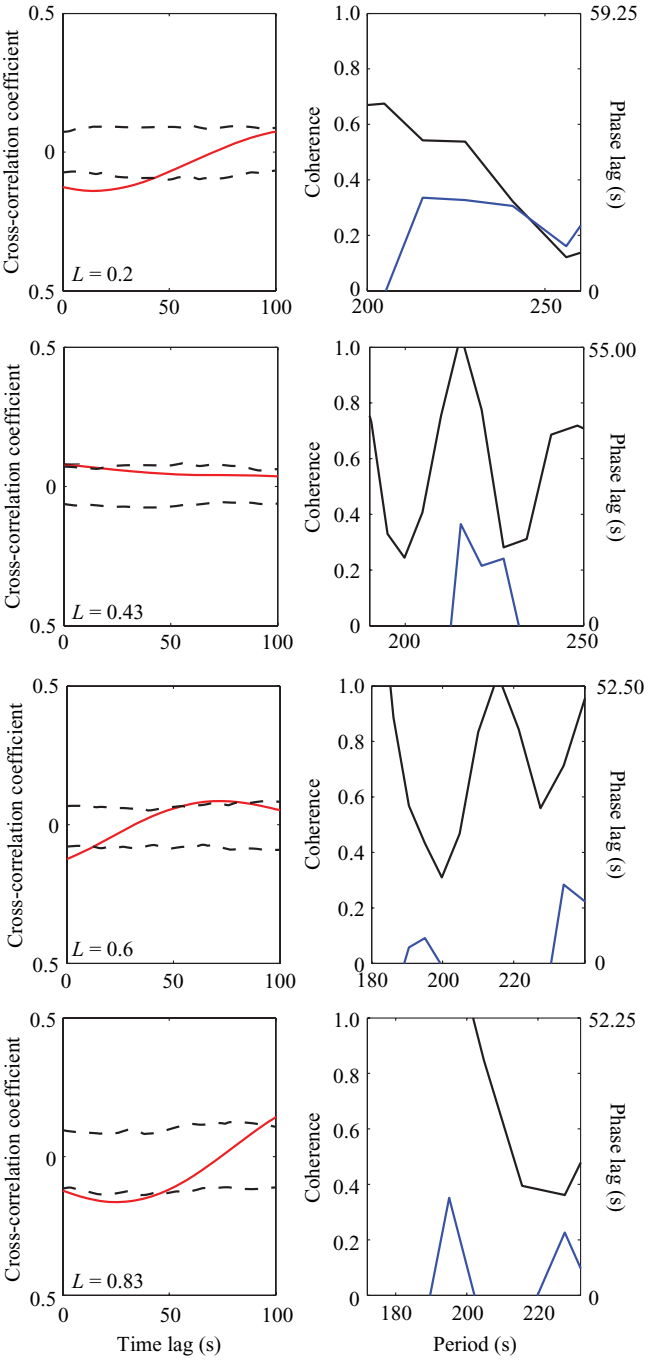

FIGURE 13. Cross-correlations (left) and analysis of coherence (black) and phase (blue) as a function of period (right) of the time series from thermocouples 'TC1' and 'TC2'. Also shown in the right panel are the estimated periods for hot thermal formation derived from the results in figure 5. Uncertainties in the time lags from the cross-correlations are calculated using the method of Saar & Manga (2004).

the power $A_{xy}(\omega)^2 = \mathrm{Re}(\Phi_{xy}(\omega))^2 + \mathrm{Im}(\Phi_{xy}(\omega))^2$. The coherence and phase spectra are, in turn,

$$\Gamma(\omega) = \frac{A_{xy}(\omega)^2}{\Phi_{xx}(\omega)\Phi_{yy}(\omega)}, \tag{A 2}$$

and

$$\varphi(\omega) = \tan^{-1}\left(\frac{\mathrm{Im}(\Phi_{xy}(\omega)}{Re(\Phi_{xy}(\omega))}\right), \tag{A 3}$$

where repeated indexes refer to autospectra. Taken together the coherence and phase spectra include the same information as the cross-correlation function but have the advantage of providing a measure of the correlation between signals as an explicit function of component frequency. This feature is particularly useful when the time series contain multiple periods that are similar. The main limitation of this technique, and reason for also cross-correlating the time series, is that the accuracy depends on the spectral resolution. The phase spectra are related to the time lag from the cross-correlation τ

$$\varphi(\omega) = \frac{2\pi\tau}{\tau_c}, \tag{A 4}$$

where τ_c is the characteristic period identified. The coherence and phase for hot periods are shown in figure A2 and are consistent with the cross-correlation analysis at the time lags indicated.

REFERENCES

Aargard, K. & Carmack, E. C. 1989 The role of sea ice and other fresh water in Arctic circulation. *J. Geophys. Res.-Climate* **94**, 14485–14498.

Aargard, K. & Carmack, E. C. 1994 The Arctic ocean and climate: a perspective. In *The Polar Oceans and Their Role in Shaping the Global Environment*, Geophysical Monograph 85, American Geophysical Union.

Blackenbach, A., Busse, F., Christensen, U. , Cserepes, L., Gunkel, D., Hansen, U., Harder, H., Jarvis, G., Koch, M., Marquart, G., Moore, D., Olson, P., Schmeling, H. & Schnaubelt, T. 1989 A benchmark comparison for mantle convection codes. *Geophys. J. Intl* **98**, 23–38.

Booker, J. R. 1976 Thermal convection with strongly temperature-dependent viscosity. *J. Fluid Mech.* **76**, 741–754.

Christensen, U. R. 1984 Heat transport by variable viscosity convection. *Phys. Earth Planet. Inter.* **35**, 264–282.

Davaille, A. & Jaupart, C. 1993 Transient high Rayleigh number convection with large viscosity variations. *J. Fluid Mech.* **253**, 141–166.

Davis, E. E. & Chapman, D. S. 1989 Heat flow variations correlated with buried basement topography on the Juan de Fuca ridge flank. *Nature* **342**, 533–37.

Donaldson, I. G. 1982 Heat and mass circulation in geothermal systems. *Annu. Rev. Earth Planet. Sci.* **10**, 377–395.

Elder, J. W. 1981 *Geothermal Systems*. Academic Press.

Giannandrea, E. & Christensen, U. 1993 Variable viscosity convection experiments with a stress-free upper boundary and implications for the heat transport in the Earth's mantle. *Phys. Earth. Planet. Inter.* **78**, 139–147.

Gloersen, P., Campbell, W. J. Cavalieri, D. J., Comiso, J. C., Parkinson, C. L. & Zwally, H. J. 1992 Arctic and Antarctic sea ice, 1978–1987: satellite and passive microwave observations and analysis. *NASA SP-511*, National Air and Space Administration. NASA: Washington, DC, 290 pp.

Gonnermann, H. M., Jellinek, A. M., Richards, M. A. & M. Manga 2004 Modulation of mantle plumes and heat flow at the core–mantle boundary by plate-scale flow: results from laboratory experiments. *Earth Planet. Sci. Lett.* **226**, 53–67.

Grigne, C. & Labrosse, S. 2001 Effects of continents on Earth cooling: thermal blanketing and depletion in radioactive elements *Geophys. Res. Lett.* **28**, 2707–2710.

Grigne, C., Labrosse, S. & P. J. Tackley 2005 Convective heat transfer as a function of wavelength: implications for the cooling of the Earth. *J. Geophys. Res.* **110**, B03409. doi: 10.1029/2004JB003376.

Guillou, L. & Jaupart, C. 1995 On the effect of continents on mantle convection. *J. Geophys. Res.* **100**, 24217–24238.

Gurnis, M. 1988 Large-scale mantle convection and the aggregation and dispersal of supercontinents. *Nature* **332**, 695–699.

Hartline, B. K. & Lister, C. R. B. Topographic forcing of supercritical convection in a porous medium such as the oceanic crust. *Earth Planet. Sci. Lett.* **55**, 75–86.

Howard, L. N. 1964 Convection at high Rayleigh number. In *Proceedings of 11th International Congress of Applied Mechanics* (ed. H. Gortler). Springer.

Incropera, F. P. & Dewitt, D. P. 1996 *Fundamentals of Heat and Mass Transfer*. John Wiley & Sons.

Jellinek, A. M., Gonnermann, H. M. & Richards, M. A. 2003 Plume capture by divergent plate motions: implications for the distribution of hotspots, geochemistry of mid-ocean ridge basalts, and estimates of the heat flux at the core-mantle boundary. *Earth Planet. Sci. Lett.* **205**, 361–378.

Jellinek, A. M., Lenardic, A. & Manga, M. 2002 The influence of interior mantle temperature on the structure of plumes: Heads for Venus, Tails for the Earth. *Geophys. Res. Lett.* **29**. doi: 10.1029/2001GL014624.

Jellinek, A. M. & Manga, M. 2002 The influence of a chemical boundary layer on the fixity, spacing and lifetime of mantle plumes. *Nature* **418**, 760–763.

Jellinek, A. M. & Manga, M. 2004 Links between long-lived hot spots, mantle plumes, D" and plate tectonics. *Rev. Geophys.* **42**, RG3002. doi: 10.1029/2003RG000144.

King, S. D. & Ritsema, J. 2000 African hotspot volcanism: small-scale convection in the upper mantle beneath cratons. *Science* **290**, 1137–1140.

Korenaga, J. & Jordan, T. H. 2004 Physics of multiscale convection in Earth's mantle: Evolution of sublithospheric convection. *J. Geophys. Res.* **109**, B01405. doi: 10.1029/2003JB002464.

Lathi, B. P. 1965 *Linear Systems and Signals*. Oxford University Press.

Lenardic, A. & Moresi, L.-N. 2003 Thermal convection below a conducting lid of variable extent: heat flow scalings and two-dimensional, infinite Prandtl number numerical simulations. *Phys. Fluids* **15**, 455–466.

Lenardic, A., Moresi, L.-N., Jellinek, A. M. & Manga, M. 2005 Continental insulation, mantle cooling, and the surface area of oceans and consitnents. *Earth Planet. Sci. Lett.* **234**, 317–333.

Lister, C. R. B. 1972 On the thermal balance of a mid-ocean ridge. *Geophys. J. R. Astr. Soc.* **26**, 515–535.

Lister, C. R. B. 1990*a* An explanation for the multivalued heat-transport found experimentally for convection in a porous medium. *J. Fluid Mech.* **214**, 287–320.

Lister, C. R. B. 1990*b* Thermal leakage from beneath sedimentary basins – an experimental test of the contribution of convective flow structures. *Earth Planet. Sci. Lett.* **99**, 133–140.

Lister, C. R. B. 1995 Heat transfer between magmas and hydrothermal systems, or 6 Lemmas in search of a theorem. *Geophys. J. Intl* **120**, 45–59.

Lowell, R. P. & Burnell, D. K. 1991 Mathematical modeling of conductive heat transfer from a freezing, convecting magma chamber to a single pass hydrothermal system: implications for seafloor black smokers. *Earth Planet. Sci. Lett.* **104**, 59–69.

Manga, M. & Weeraratne, D. 1999 Experimental study of non-Boussinesq Rayleigh–Benard convection at high Rayleigh and Prandtl numbers. *Phys. Fluids* **11**, 2969–2976.

Manga, M., Weeraratne, D. & Morris, S. J. S. 2001 Boundary layer thickness and instabilities in Benard convection of a liquid with a temperature-dependent viscosity. *Phys. Fluids* **13**, 802–805.

Moresi, L.-N. & Solomatov, V. S. 1995 Numerical investigation of 2D convection with extremely large viscosity variations. *Phys. Fluids* **7**, 2154–2162.

Moresi, L.-N. & Solomatov, V. S. 1998 Mantle convection with a brittle lithosphere: thoughts on the global tectonic style of the Earth and Venus. *Geophys. J.* **133**, 669–682.

Morris, S. & Canright, D. 1984 A boundary-layer analysis of Bernard convection in a fluid of strongly temperature-dependent viscosity. *Phys. Earth. Planet. Intl* **36**, 355–373.

Niemela, J. J., Skrbek, L., Sreenivasan, K. R. & Donnelly, R. J. 2000 Turbulent convection at very high Rayleigh numbers. *Nature* **404**, 837–840.

Norton, D. 1984 A theory of hydrothermal systems. *Annu. Rev. Earth Planet. Sci.* **12**, 155–177.

Ogawa, M., Schubert, G. & Zebib, A. 1991 Numerical simulation of three-dimensional thermal convection in a fluid with strongly temperature-dependent viscosity. *J. Fluid Mech.* **233**, 299–328.

Park, J., Lindberg, C. R. & Vernon, F. L. III 1987 Multitaper spectral analysis of high-frequency seismograms. *J. Geophys. Res.* **92**, 12675–12684.

Parkinson, C. L. 1997 *Earth From Above: Using Color-Coded Satellite Images to Examine the Global Environment*. University Science Books.

Parkinson, C. L., Comiso, J. C., Zwally, H. Z., Cavalleri, D. J., Gloersen, P. & Campbell, W. J. 1987 Arctic sea ice, 1973–1976. *NASA SP-489*, National Air and Space Administration.

Person, M., Raffensperger, J. P., Ge, S. & Garven, G. 1996 Basin-scale hydrogeologic modeling. *Revs. Geophys.* **34**, 61–88.

Richter, F. M., Nataf, H. C. & Daly, S. F. 1983 Heat transfer and horizontally-averaged temperature of convection with large viscosity variations. *J. Fluid Mech.* **129**, 173–192.

Robin, C. M. I., Jellinek, A. M., Thayalan, V. & Lenardic, A. 2007 Transient mantle convection on Venus: the paradoxical coexistence of highlands and coronae in the BAT region. *Earth Planet. Sci. Lett.* **256**, 100–119.

Saar, M. O. & Manga, M. 2004 Depth dependence of permeability in the Oregon Cascades inferred from hydrogeologic, thermal, seismic, and magmatic modeling constraints. *J. Geophys. Res.* **109** (B4), B04204. doi: 10.1029/2003JB002855.

Schaeffer, N. & Manga, M. 2001 Interactions between rising and sinking mantle plumes. *Geophys. Res. Lett.* **28**, 455–458.

Sleep, N. H. & Jellinek, A. M. 2008 Scaling relationships for chemical-lid convection with applications to cratonal lithosphere. *Geochem. Geophys. Geosyst.* **9**, Q12025. doi: 10.1029/2008GC002042.

Solomatov, V. S. 1995 Scaling of temperature- and stress-dependent viscosity convection. *Phys. Fluids* **7**, 266–274.

Solomatov, V. S. & Moresi, L.-N. 1996 Stagnant lid convection on Venus. *J. Geophys. Res.* **101**, 4737–4753.

Solomatov, V. S. & Moresi, L.-N. 2000 Scaling of time-dependent stagnant lid convection: application to small-scale convection on Earth and other terrestrial planets. *J. Geophys. Res.* **105** 21795–21817.

Stengel, K. C., Oliver, D. S. & Booker, J. R. 1982 Onset of convection in a variable-viscosity fluid. *J. Fluid Mech.* **120**, 411–431.

Thayalan, V., Jellinek, A. M. & Lenardic, A. 2006 Recycling the lid: Effects of subduction and stirring on boundary layer dynamics in bottom-heated planetary mantle convection. *Geophys. Res. Lett.* **33**, L20318, doi:10.1029/2006GL027668.

Thomson, D. J. 1982 Spectrum estimation and harmonic analysis. *Proc. IEEE* **70**, 1055–1096.

Trompert, R. A. & Hansen, U. 1998 On the Rayleigh number dependence of convection with a strongly temperature-dependent viscosity. *Phys. Fluids* **10**, 351–360.

Welch, P. D. 1967 The use of fast Fourier transform for the estimation of power spectra: a method based on time averaging over short, modified periodograms. *IEEE Trans. Audio Electroacoust.* **AU-15**, 70–73.

Weeraratne, D. & Manga, M. 1998 Transitions in the style of mantle convection at high Rayleigh numbers, *Earth Planet. Sci., Lett.* **160**, 563–568.

Zhang, J., Childress, S. & Libchaber, A. 1997 Non-Boussinesq effect: thermal convection with broken symmetry. *Phys. Fluids* **9**, 1034.

Zhang, J. & Libchaber, A. 2000 Periodic boundary motion in thermal turbulence. *Phys. Rev. Lett.* **84**, 4361–4364.

Zhong, S. & Gurnis, M. 1993 Dynamic feedback between a continent-like raft and thermal convection. *J. Geophys. Res.* **98**, 12219–12232.